

Improved Determination of Subnuclear Position Enabled by Three-Dimensional Membrane Reconstruction

Yao Zhao,¹ Sarah M. Schreiner,² Peter K. Koo,³ Paolo Colombi,² Megan C. King,^{2,*} and Simon G. J. Mochrie^{1,3,*}

¹Department of Applied Physics, ²Department of Cell Biology, Yale School of Medicine, and ³Department of Physics, Yale University, New Haven, Connecticut

ABSTRACT Many aspects of chromatin biology are influenced by the nuclear compartment in which a locus resides, from transcriptional regulation to DNA repair. Further, the dynamic and variable localization of a particular locus across cell populations and over time makes analysis of a large number of cells critical. As a consequence, robust and automatable methods to measure the position of individual loci within the nuclear volume in populations of cells are necessary to support quantitative analysis of nuclear position. Here, we describe a three-dimensional membrane reconstruction approach that uses fluorescently tagged nuclear envelope or endoplasmic reticulum membrane marker proteins to precisely map the nuclear volume. This approach is robust to a variety of nuclear shapes, providing greater biological accuracy than alternative methods that enforce nuclear circularity, while also describing nuclear position in all three dimensions. By combining this method with established approaches to reconstruct the position of diffraction-limited chromatin markers—in this case, lac Operator arrays bound by lacI-GFP—the distribution of loci positions within the nuclear volume with respect to the nuclear periphery can be quantitatively obtained. This stand-alone image analysis pipeline should be of broad practical utility for individuals interested in various aspects of chromatin biology, while also providing, to our knowledge, a new conceptual framework for investigators who study organelle shape.

INTRODUCTION

Nuclear compartmentalization is essential for many nuclear processes and functions (1,2). The nuclear envelope (NE) physically associates with heterochromatin, linking it to gene-poor and silenced regions of the genome, supporting heterochromatinization and genome stability (2,3). In addition, genes from the nucleoplasm can be recruited to nuclear pore complexes through interactions with *cis*-acting DNA “zip-codes” (4). This recruitment to the periphery corresponds to gene activation in yeast, and may act to regulate the kinetics of gene induction and repression, as well as gene “memory” (4–6).

To visualize specific genes in live yeast, researchers often use engineered genomic integrants of tandem lac Operator (lacO) or tet Operator (tetO) arrays in cells expressing fluorescently tagged cognate repressors (7,8). Importantly, existing approaches discard three-dimensional (3D) infor-

mation about the localization of the lacO or tetO arrays and assume that the nucleus is a sphere (9–11), which is rarely sufficient to describe the true nuclear volume, particularly in fission yeast (12). A more precise and scalable approach is to fit the 3D location of lacO or tetO arrays at subdiffraction resolution, reconstruct the shape of the NE, and measure the localization relation between these two. Reconstructing an accurate 3D surface from a fluorescently labeled membrane structure, such as the NE, represents a key challenge to such an approach. The traditional slice-by-slice method of membrane reconstruction takes a stack of images with a set separation (z-stack), then uses edge-detection techniques to extract the two-dimensional (2D) contour of the membrane in each image, and finally reconstructs these contours at each plane to give a 3D shape (13). However, this approach often fails to fit a subset of z-slices, thereby compromising the ability to reconstruct true 3D volume (14). This problem is particularly severe for the z-slices at the top and bottom of the NE, because the NE is nearly parallel to the image plane in these regions. Alternatively, 2D edge detection operations can be scaled to a 3D image matrix (14); however, such edge-detection approaches are

Submitted September 25, 2015, and accepted for publication May 11, 2016.

*Correspondence: megan.king@yale.edu or simon.mochrie@yale.edu

Yao Zhao and Sarah M. Schreiner contributed equally to this work.

Editor: David Piston.

<http://dx.doi.org/10.1016/j.bpj.2016.05.036>

© 2016 Biophysical Society.

best suited for volumetric data, where the interior of the object of interest has a uniform intensity with high contrast to the surrounding medium.

Here, we describe a method that can robustly reconstruct the shape of a fluorescently labeled organelle membrane by using either a predefined or a dynamically generated 3D surface framework that is fit to a full z-stack of images with subpixel resolution using maximum a posteriori (MAP) estimation. This approach is capable of reconstructing a wide range of volumetric shapes, including the most distal axial regions captured at the uppermost and lowermost Z-planes, from 3D data of fluorescently labeled membrane structures with different noise levels and labeling conditions. Combined with 3D particle localization of genetic loci, these precisely reconstructed NE shapes also provide a coordinate system for quantitatively studying nuclear compartmentalization. Because of the flexibility of this approach, we expect that it will be of utility in quantitatively defining organelle shape in many areas of cell biological research.

MATERIALS AND METHODS

Yeast cell culture and strain generation

The strains used in this study are listed in Table S1 in the [Supporting Material](#). *Schizosaccharomyces pombe* cells were grown and maintained in standard cell culture conditions (15). All strains were grown at 30°C. The AscIcs-Ura-LacO-10.3kb plasmid was used for lacO integration (16). Methods adapted from *S. cerevisiae* were used for lacO integration into the *pst1*, *spf38*, and *mmf1* loci (17). All strains generated by cassette integration were confirmed by PCR. Strains made through genetic crosses were confirmed by the segregation of markers and/or by the presence of the appropriate fluorescently tagged protein. *S. cerevisiae* strains were grown to mid-log phase in YPAD (1% yeast extract, 2% peptone, 2% dextrose, 0.025% adenine) at 30°C.

Mammalian cell line derivation and cell culture

Immortalized NIH/3T3 mouse embryonic fibroblasts (MEFs) stably expressing GFP-mini-Nesprin2G (18) were cultured at 37°C and 5% CO₂ in high glucose Dulbecco's Modified Eagle's Medium (Life Technologies/Thermo Fisher Scientific, Waltham, MA), supplemented with 10% fetal bovine serum (Life Technologies/Thermo Fisher Scientific) and 5% penicillin/streptomycin (Life Technologies). This MEF line was created through transient transfection of GFP-miniNesprin2G (provided by Gregg Gundersen; Columbia University, New York, NY) using jetPRIME transfection reagent (Polyplus-transfection, Illkirch-Graffenstaden, France) according to the manufacturer's instructions, followed by selection with 1200 µg/mL geneticin. Briefly, MEFs grown in serum-containing medium were grown in 100-mm dishes and exposed to 10 µg GFP-miniNesprin2G plasmid in the presence of 500 µL jetPRIME buffer and 20 µL jetPRIME reagent. Forty-eight hours post-transfection, cells were grown in medium containing 1200 µg/mL geneticin; this selection was maintained until stable integrants were derived.

Microscopy

S. pombe strains were grown in YE5S plus 250 mg/L adenine to log phase (OD600 0.5–0.8). Cells were mounted on agarose pads (1.4% agarose in Edinburgh minimal media) and sealed with VALAP (1:1:1, Vaseline/

lanolin/paraffin). *S. cerevisiae* strains were grown to log phase in YPAD (1% yeast extract, 2% peptone, 2% dextrose, 0.025% adenine) at 30°C and rinsed in complete synthetic medium containing 2% dextrose and 0.025% adenine. Cells were mounted on 1.4% agarose pads containing complete synthetic medium and 2% dextrose and sealed with VALAP. For imaging of mammalian nuclei, MEFs stably expressing GFP-miniNesprin2G were grown on 35-mm glass-bottom dishes (P35G-0.170-14-C; MatTek, Ashland, MA) coated in 50 µg/mL fibronectin (Sigma-Aldrich, St. Louis, MO) in culture media supplemented with 25 mM HEPES (Sigma-Aldrich). Cells were imaged using the same instrument as for yeast. Single z-stacks covered 15.2 µm or 17.2 µm, acquired as 0.2-µm slices. All live cell images were acquired on a Deltavision Widefield Deconvolution Microscope (Applied Precision/GE Healthcare, Issaquah, WA) with an Evolve 512 EMCCD camera (Photometrics, Tucson, AZ).

MAP estimation of membrane shape

We use a predefined spherical 3D triangle mesh network as an initial guess for datasets containing largely spherical nuclei. The mesh network is centered at each nucleus and has the size defined by the mean radius of the nucleus as measured from a 2D projection of the z-stack. For shapes that deviate largely from a sphere, such as mitotic nuclei, the initial mesh network is generated in the following steps: we first locate the voxels that correspond to the fluorescently labeled membrane, the intensity of which has the property that its second derivative along the direction perpendicular to the membrane has a large negative value, while its second derivatives along directions parallel to the membrane are approximately zero. A 3D triangle mesh representing a 3D surface is generated from the locations of those voxels. To reduce the complexity of the mesh, we apply an iterative balancing algorithm that adjusts the edge lengths and the mesh connectivity to uniformly sample the membrane. The detailed process is described in the [Supporting Material](#).

To infer the posterior probability of the 3D mesh network (M) from a given image z-stack (Z), namely $P(M|Z)$, we invoke Bayes' theorem, which informs us that the posterior probability is proportional to:

$$P(M|Z) \propto P(M)P(Z|M), \quad (1)$$

where $P(Z|M)$ is the likelihood of the z-stack given the mesh network, and $P(M)$ is the prior probability of the mesh.

Maximizing the posterior probability seeks to determine the vertex coordinates, $\{\mathbf{r}_i\}$, and the corresponding vertex intensities, $\{I_i\}$. To simplify the optimization procedure, we impose the constraint that the number of vertices, and thus the number of triangles, and their connections, are held constant. Thus, we may rewrite (Eq. 1) as

$$P(\{\mathbf{r}_i, I_i\} | \{I_m(\mathbf{r})\}) \propto P(\{\mathbf{r}_i, I_i\})P(\{I_m(\mathbf{r})\} | \{\mathbf{r}_i, I_i\}), \quad (2)$$

where $\{I_m(\mathbf{r})\}$ is the set of intensities measured at each voxel \mathbf{r} in the z-stack.

The likelihood of realizing voxel intensities given a mesh shape and fluorophore intensity depends on the PSF and the image acquisition noise:

$$P(\{I_m(\mathbf{r})\} | \{\mathbf{r}_i, I_i\}) = \prod_{\mathbf{r}} \frac{1}{\sqrt{2\pi\sigma(\mathbf{r})^2}} e^{-\frac{(I_m(\mathbf{r}) - I(\mathbf{r}))^2}{2\sigma(\mathbf{r})^2}}, \quad (3)$$

where $I(\mathbf{r})$ is the intensity at voxel \mathbf{r} , determined from the convolution of the PSF and the mesh, $\{\mathbf{r}_i, I_i\}$; and $\sigma(\mathbf{r})$ is the standard deviation of the errors at voxel \mathbf{r} .

Without knowledge of the fluorophore distribution, the prior probability only depends on the membrane shape, which follows a Boltzmann distribution for thermally excited membranes according to:

$$P(\{\mathbf{r}_i\}) \propto e^{-H/(k_B T)}, \quad (4)$$

where H is the membrane bending energy given by the Helfrich-Canham-Evans Hamiltonian (19). However, if membrane fluctuations are excited by additional nonthermal noise sources like metabolic forces, we may expect the form of the prior to be the same as in Eq. 4, but with a modified temperature, provided the additional noise is sufficiently spatially uniform. Importantly, this form for the prior serves as a regularization term that prevents overinterpreting a noisy image z-stack.

To determine the MAP estimate, we apply a gradient-descent numerical search procedure to find the mesh surface that maximizes the posterior probability directly, or equivalently, minimizes the negative logarithm of the posterior probability. (See the [Supporting Material](#).) Software implementing these methods is available to download at GitHub (<https://github.com/mochriellab/3DMembraneReconstruction>).

lacO array particle localization

A small 3D region-of-interest, centered on each fluorescent lacO array, is cropped from the full z-stack of images by intensity maxima detection and its background is removed. Localization of the lacO array is then performed by applying a least-squares minimization between the cropped z-stack images and the intensity profile of a point particle convoluted with the microscope PSF (20,21).

RESULTS AND DISCUSSION

Approach to 3D NE reconstruction

To visualize the NE, we imaged fission yeast strains expressing the Cut11-GFP nucleoporin from its endogenous locus. Three-dimensional structural information of individual nuclei is encoded in 2D sequential microscope images collected at different focal depths (z-slices), to give a z-stack. We used a z-slice spacing of 200 nm, approximately equal to one-third the axial resolution of the microscope. Here, 25 z-slices are sufficient to capture the total axial range of the nuclear volume, as *Schizosaccharomyces pombe* nuclei are typically ~2–3 μm in diameter (Fig. 1 A).

As a result of its association with nuclear pore complexes, Cut11 is not uniformly distributed across the NE, resulting in uneven fluorescent intensity along the nuclear contour with a low signal/noise in some regions (Fig. 1, A and B). Such variation in image intensity hinders most previously described methods for accurately determining the location of the NE. To overcome this challenge, we represent the shape of the NE by a 3D mesh of triangles with intensity values that represent a fluorophore density assigned to each vertex, automatically accounting for this inhomogeneity. Our method to infer the triangle mesh representation from a z-stack of images occurs in two steps: (1) from the z-stack, we determine an initial 3D triangle representation of the membrane surface; and (2) using the initial 3D triangle mesh, we then find the MAP membrane that best represents the z-stack. (See Materials and Methods.) As shown in the [Supporting Material](#), by examining the performance of our 3D membrane reconstruction method, applied to realistic simulated z-stacks, we conclude that our method is able to localize the membrane within ± 30 nm.

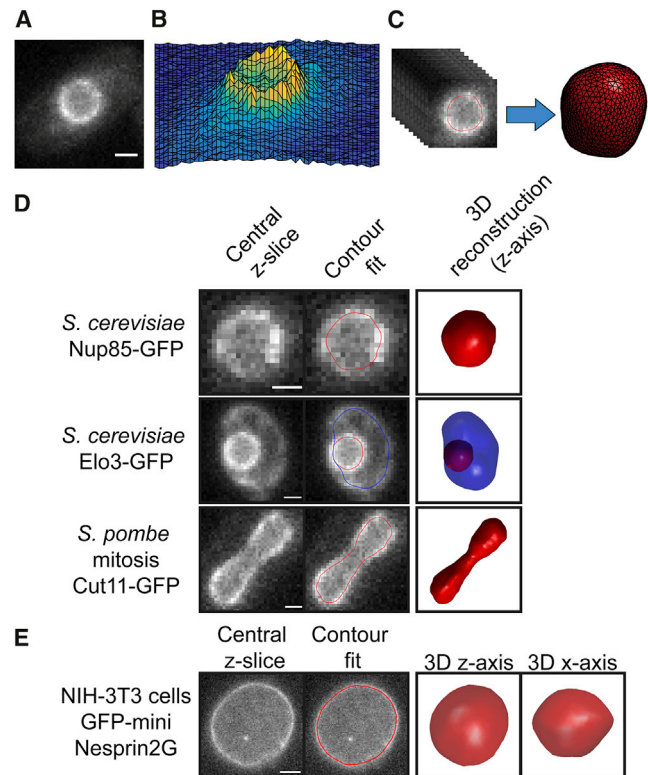


FIGURE 1 The 3D nuclear volume can be reconstructed using a triangular-mesh-based approach. (A) Fluorescence micrograph of an *S. pombe* cell expressing Cut11-GFP, which localizes to the NE, in the central z-plane. (B) Surface plot derived from the image in (A), revealing the nonuniformity of the Cut11-GFP signal within the NE. (C) A full z-stack of images is used to reconstruct the NE contour using a 3D mesh of triangles that are inferred using MAP estimation. (D) Central z-slices (first column) of a budding yeast cell expressing NE marker Nup85-GFP (top) or ER marker Elo3-GFP (middle), and of a mitotic fission yeast nucleus expressing Cut11-GFP (bottom). The second and third columns include the contour(s) of the reconstructed membrane(s) and the 3D membrane reconstruction, respectively. (E) Central z-slice (first column) of a mouse embryonic fibroblast expressing GFP-mini-Nesprin-2G. The second, third, and fourth columns include the contour of the reconstructed membrane, with the 3D membrane reconstruction looking from the z axis and the x axis. The scale bars represent 1.6 μm (A), 1.0 μm (D), and 5.0 μm (E). To see this figure in color, go online.

Broad applicability of the approach

We also investigated whether the same approach is able to reconstruct nuclear shape in budding yeast and mammalian cells. Contours derived from image stacks of *Saccharomyces cerevisiae* nuclei expressing either the nucleoporin Nup85-GFP, or Elo3-GFP, an endoplasmic reticulum (ER) protein, can be efficiently described using the same experimental approach (Fig. 1 D, row 2). Remarkably, the 3D membrane reconstruction could be segmented to separately delineate the cortical ER (blue contour in this figure) from the NE (red contour), with the one drawback that where the cortical ER is close to the NE, the reconstruction is biased toward the NE and does not properly capture the dimmer cortical ER in this limited region. However, the reconstruction of the NE remains robust under these conditions.

Next, we examined how well the algorithm can reconstruct 3D membrane shapes that deviate radically from spheres. During *S. pombe* mitosis, the NE is greatly stretched by the growing mitotic spindle (Fig. 1 D, row 3). Gratifyingly, the contours of the nucleus as it elongates during mitosis were efficiently described by our approach (Figs. 1 D and S2).

Finally, to investigate the method's utility in mammalian cells we expressed GFP-miniNesprin-2G (18), which localizes to the NE, in mouse embryonic fibroblasts. In this case too, although the size scale is approximately fivefold larger than for yeast nuclei, our method readily reconstructs the 3D nuclear volume (Fig. 1 E), including the flattened nuclear surface on the basal side that is typical of many adherent mammalian cell lines.

3D subnuclear localization of tagged loci

Although several 2D methods (or 3D methods that utilize nuclear landmarks in budding yeast, but which cannot be used in other model organisms) exist (10,22), there is a need for a broadly applicable, 3D method that can capture gene position within the true nuclear volume. Thus, we next sought to take advantage of our membrane reconstruction approach to provide an appropriate coordinate system within which specific gene loci could be treated as subdiffraction particles to precisely locate their positions in 3D.

To fluorescently tag genomic loci, we integrated lacO arrays at several positions in the *S. pombe* genome (16) in strains expressing lacI-GFP and Cut11-mCherry, including lacO integrations next to the loci *mmf1*, *pst1*, *cut3*, and *spf38* (Fig. 2). Fig. 2 A shows a representative central z-slice from a cell of each strain (left) and 3D renderings of the same cells (right) from three orthogonal viewpoints. We represent the lacO volume in green with the dimensions of the PSF and the NE membrane reconstruction in red.

To date, one of the most commonly used methods for describing the distribution of fluorescently tagged gene loci within the nucleus is a three-zone system, in which a single 2D focal plane of a z-stack is analyzed with respect to three rings of equal area (Fig. 2 B; (10,23)). One major caveat to this approach is the assumption that nuclei are spherical, which is not accurate for most model systems. Further, if such an approach is applied to projected image stacks, loci may be erroneously assigned as residing in the center of the nucleus (Zone 3), even if their location is at the nuclear periphery (Zone 1; Fig. 2, B and C). The worst inaccuracies can be avoided by modifying the 2D three-zone approach to use the z-plane in which a locus' fluorescent signal is most intense, that is, the best in-focus z-slice. However, even in this case, there remain issues when the position of the locus is far above or far below the nucleus' central z-slice, leading to decreased accuracy, due to increased distance measurement bias (Fig. 2 C).

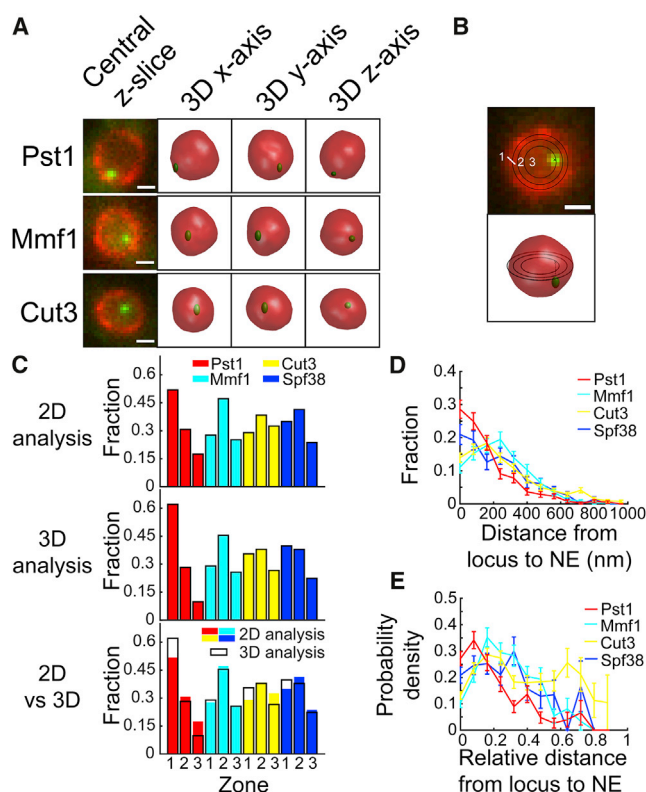


FIGURE 2 Three-dimensional membrane reconstruction greatly enhances the precision of subnuclear locus localization. (A) Examples of a central z-slice (first column) and reconstructed 3D nuclear volumes viewed from the perspective of the three orthogonal axes (second, third, and fourth columns). Each representative cell is expressing Cut11-mCherry and lacI-GFP. Lac operator arrays were integrated at three loci that represent different distributions within the nucleus: *pst1* (top), *mmf1* (middle), and *cut3* (bottom). The lacO-lacI-GFP focus is rendered based on its treatment as a diffraction-limited particle. (B) Comparison of a three-zone system applied to a projected 2D image of a cell expressing Cut11-mCherry and containing a lacO-lacI-GFP focus (top) and the true nuclear position of the lacO array in the 3D nuclear volume (bottom). Zones 1, 2, and 3 represent shells of equal area. (C) Analysis of the subnuclear position of four loci, *pst1*, *mmf1*, *cut3*, and *spf38*, using the three-equal-area zone system applied to central 2D z-slices (top) or using a three equal-volume zone system based on 3D reconstructed membranes (bottom). Even though our method reveals that the lacO array, integrated at *pst1*, is preferentially associated with the nuclear periphery, in many cells this peripheral position is incorrectly assigned to the central zone by the 2D method. Similarly, the distribution of *cut3* is distorted by the 2D method. (D) Distribution of the distance between the lacO array integrated at each of the four loci and the NE derived from our 3D reconstructions. Here, *pst1* is enriched at the NE and is depleted from the nuclear interior, while both *mmf1* and *cut3* are depleted near the NE. Here, *spf38* shows an intermediate distribution, being enriched at the NE but more evenly distributed within the nuclear interior compared to *pst1*. Error bars correspond to the square root of the number of nuclei in each bin. (E) Probability density plotted as a function of the locus to NE distance relative to the mean nuclear radius. This representation reveals a nearly uniform distribution for *cut3*, while *pst1* is strongly biased toward the nuclear periphery. Here, *mmf1* appears more constrained than *cut3*, being relatively depleted from the center of the nucleus, while *spf38* has an intermediate distribution. Error bars correspond to the square root of the number of nuclei in each bin. For all panels (C–E), the total number of nuclei were 385 (*pst1*), 380 (*mmf1*), 660 (*cut3*), and 229 (*spf38*). (A and B) The scale bars represent 1 μ m. To see this figure in color, go online.

Alternatively, data from distal imaging planes can be discarded, at the cost of increasing the number of images that must be acquired to properly sample positional distributions. These issues are avoided with the 3D reconstruction (Fig. 2 A), described here. Consistent with these expectations, the same data set, analyzed using either the best-in-focus-z-slice 2D method (Fig. 2 C, top) or our 3D method (Fig. 2 C, middle), reveals that the 2D method leads to significantly distorted zone distributions (Fig. 2 C, bottom), with the largest discrepancy occurring for loci that have a high probability of residing at the nuclear periphery, as predicted (*pst1*; Fig. 2 D). Beyond this improved accuracy, key advantages of our 3D method include its robustness, its capability of reconstructing the top and bottom slices of a stack of images, and its adaptability to different imaging conditions. For example, in the case of the *S. pombe* NE, inhomogeneously labeled with Cut11-GFP, most cells fail to be reconstructed in more than one of their z-slices using 2D slice-by-slice methods. By contrast, our approach readily reconstructs such membranes.

The approach described here can readily assess locus position within the nucleus without dividing it into volumes, because the distribution of lacO array positions in a cell population can be interrogated directly. Measurements of the shortest distances from the lacO array to the NE in populations of cells for each integration site are represented as histograms with a binning size of 80 nm in Fig. 2 D. The estimated localization errors of the lacO array and the NE are 25 and 30 nm, respectively, leading to a total localization error of 40 nm; the chosen bin size is therefore twice the localization error. The resulting histograms show how likely it is that each locus will be found a given distance away from the NE. Plotted in this way, it is clear that *pst1* is most likely to be strongly associated with the nuclear periphery, while *mmf1* and *cut3* sample significantly more of the nuclear volume (Fig. 2 D). The distribution of *spf38* is more complex, having attributes in common with both *pst1* (that is, a greater likelihood to be found at the NE) and *mmf1/cut3* (that is, it also samples the nuclear interior), raising the possibility that this locus may occupy two different preferential nuclear localizations depending on some as-yet unknown variable. A direct comparison between these 3D histograms and the comparable histograms, obtained using the best-in-focus-z-slice 2D method, are presented in Fig. S3, confirming the distortion that accompanies even the best-in-focus-z-slice 2D method.

To better represent the differences in the loci distribution, the positions were normalized for average nuclear size and the probability density distribution was determined (Fig. 2 E). The probability density, $\rho(r) = P(r)/(4\pi(1-r)^2\delta r)$, specifies the probability per dimensionless nuclear volume that a gene locus is fractional r distance away from the membrane, where $r = d/R$ is the loci-to-NE distance d normalized by the nuclear radius R ; $P(r)$ is the fraction of measured loci that fall into the shell between

$[r - (\delta r/2), r + (\delta r/2)]$; and δr is the normalized thickness of the shell ($R \approx 1000$ nm, $\delta r = 0.08$).

The probability density, $\rho(r)$, for the *cut3* locus appears independent of r , suggesting that this locus is randomly distributed throughout the nuclear volume. By contrast, the probability density for the *pst1* locus exhibits a peak at or very near the NE, suggesting that this locus may be tethered to the NE in most of the population. The slowly diminishing probability density for *pst1* with increasing distance from the NE suggests that this proposed NE association may sometimes be lost, allowing this locus to move away from the NE. For the *mmf1* locus, the peak of the probability density is at ~ 0.2 fractional distance units away from the nuclear radius, which could be consistent with a tether to the NE that is some curvilinear distance along the chromosome from *mmf1*, causing its distribution to resemble that of a NE-tethered particle. As noted above, the probability density for the *spf38* locus shows attributes of both the *pst1* and *cut3* distributions. However, more data are needed to interpret what this may represent biologically. Interestingly, *cut3* and *mmf1* (and to a lesser extent *spf38*) display a clear decrease in the probability density at the NE and peak at ~ 0.2 fractional distance units from the NE. This observation is consistent with a model in which the nuclear periphery is populated with chromatin that has binding sites that promote attachment to the NE, which manifest as an apparent repulsion of unattached chromatin away from this region.

Overall, the combination of 3D nuclear volume reconstruction with tagged genomic locus position will prove a valuable tool for investigators interested in chromatin biology. In addition, our membrane reconstruction approach will be broadly applicable in experiments focusing on organelle shape.

SUPPORTING MATERIAL

Supporting Materials and Methods, four figures, and one table are available at [http://www.biophysj.org/biophysj/supplemental/S0006-3495\(16\)30361-7](http://www.biophysj.org/biophysj/supplemental/S0006-3495(16)30361-7).

AUTHOR CONTRIBUTIONS

Y.Z. developed the software and analyzed the data; S.M.S. and P.C. performed measurements; and Y.Z., S.M.S., P.K.K., P.C., M.C.K., and S.G.J.M. designed the research and wrote the article.

ACKNOWLEDGMENTS

We thank Dr. Dongxu Lin, Dr. Brant Webster, Bryan Leland, and Rachel Stewart for constructing strains and cell lines. The strain containing the lacO array at the *cut3* locus was generated by the laboratory of Dr. Yasushi Hiraoka (Osaka University).

This work was supported by National Science Foundation grant No. CMMI-1334406, an American Heart Association Founders Affiliate Pre-doctoral Fellowship No. 13PRE17070004 (to S.M.S.), National Institutes of Health grant No. T32-GM007499 (to S.M.S.), National Science

Foundation grant No. PHY 1522467 (to S.G.J.M.), the Searle Scholars Program (to M.C.K.), the National Institutes of Health grant No. DP2OD008429 (to M.C.K.), and seed funding from the Raymond and Beverly Sackler Institute for Physical and Engineering Biology at Yale.

REFERENCES

1. Mekhail, K., and D. Moazed. 2010. The nuclear envelope in genome organization, expression and stability. *Nat. Rev. Mol. Cell Biol.* 11:317–328.
2. Akhtar, A., and S. M. Gasser. 2007. The nuclear envelope and transcriptional control. *Nat. Rev. Genet.* 8:507–517.
3. Mekhail, K., J. Seebacher, ..., D. Moazed. 2008. Role for perinuclear chromosome tethering in maintenance of genome stability. *Nature.* 456:667–670.
4. Ahmed, S., D. G. Brickner, ..., J. H. Brickner. 2010. DNA zip codes control an ancient mechanism for gene targeting to the nuclear periphery. *Nat. Cell Biol.* 12:111–118.
5. Taddei, A. 2007. Active genes at the nuclear pore complex. *Curr. Opin. Cell Biol.* 19:305–310.
6. Ibarra, A., and M. W. Hetzer. 2015. Nuclear pore proteins and the control of genome functions. *Genes Dev.* 29:337–349.
7. Straight, A. F., A. S. Belmont, ..., A. W. Murray. 1996. GFP tagging of budding yeast chromosomes reveals that protein-protein interactions can mediate sister chromatid cohesion. *Curr. Biol.* 6:1599–1608.
8. Michaelis, C., R. Ciosk, and K. Nasmyth. 1997. Cohesins: chromosomal proteins that prevent premature separation of sister chromatids. *Cell.* 91:35–45.
9. Nagai, S., K. Dubrana, ..., N. J. Krogan. 2008. Functional targeting of DNA damage to a nuclear pore-associated SUMO-dependent ubiquitin ligase. *Science.* 322:597–602.
10. Hediger, F., A. Taddei, ..., S. M. Gasser. 2004. Methods for visualizing chromatin dynamics in living yeast. *Methods Enzymol.* 375:345–365.
11. Brickner, D. G., W. Light, and J. H. Brickner. 2010. Quantitative localization of chromosomal loci by immunofluorescence. *Methods Enzymol.* 470:569–580.
12. Schreiner, S. M., P. K. Koo, ..., M. C. King. 2015. The tethering of chromatin to the nuclear envelope supports nuclear mechanics. *Nat. Commun.* 6:7159.
13. Boissonnat, J.-D. 1988. Shape reconstruction from planar cross sections. *Comput. Vis. Graph. Image Process.* 44:1–29.
14. Li, K., X. Wu, ..., M. Sonka. 2006. Optimal surface segmentation in volumetric images—a graph-theoretic approach. *IEEE Trans. Pattern Anal. Mach. Intell.* 28:119–134.
15. Moreno, S., A. Klar, and P. Nurse. 1991. Molecular genetic analysis of fission yeast *Schizosaccharomyces pombe*. *Methods Enzymol.* 194:795–823.
16. Leland, B. A., and M. C. King. 2014. Using LacO arrays to monitor DNA double-strand break dynamics in live *Schizosaccharomyces pombe* cells. *Methods Mol. Biol.* 1176:127–141.
17. Rohner, S., S. M. Gasser, and P. Meister. 2008. Modules for cloning-free chromatin tagging in *Saccharomyces cerevisiae*. *Yeast.* 25:235–239.
18. Luxton, G. W., E. R. Gomes, ..., G. G. Gundersen. 2010. Linear arrays of nuclear envelope proteins harness retrograde actin flow for nuclear movement. *Science.* 329:956–959.
19. Campelo, F., and A. Hernández-Machado. 2006. Dynamic model and stationary shapes of fluid vesicles. *Eur. Phys. J. E Soft Matter.* 20:37–45.
20. Godinez, W. J., M. Lampe, ..., K. Rohr. 2009. Deterministic and probabilistic approaches for tracking virus particles in time-lapse fluorescence microscopy image sequences. *Med. Image Anal.* 13:325–342.
21. Chenouard, N., I. Smal, ..., E. Meijering. 2014. Objective comparison of particle tracking methods. *Nat. Methods.* 11:281–289.
22. Berger, A. B., G. G. Cabal, ..., C. Zimmer. 2008. High-resolution statistical mapping reveals gene territories in live yeast. *Nat. Methods.* 5:1031–1037.
23. Taddei, A., G. van Houwe, ..., S. M. Gasser. 2006. Nuclear pore association confers optimal expression levels for an inducible yeast gene. *Nature.* 441:774–778.